

Water Resources Research

RESEARCH ARTICLE

10.1029/2017WR022476

Key Points:

- Revision of heat-pulse tracer tests theory for in situ Darcy flux determination
- Robust means of detection and delineation of three-dimensional flow fields
- Versatile tools for design of new probes and reinterpretation of existing data

Correspondence to:

D. M. Tartakovsky,
tartakovsky@stanford.edu

Citation:

Zlotnik, V., & Tartakovsky, D. M. (2018). Interpretation of heat-pulse tracer tests for characterization of three-dimensional velocity fields in hyporheic zone. *Water Resources Research*, 54, 4028–4039. <https://doi.org/10.1029/2017WR022476>

Received 23 DEC 2017

Accepted 8 MAY 2018

Accepted article online 14 MAY 2018

Published online 28 JUN 2018

Interpretation of Heat-Pulse Tracer Tests for Characterization of Three-Dimensional Velocity Fields in Hyporheic Zone

Vitaly Zlotnik¹ and Daniel M. Tartakovsky² 

¹Department of Earth and Atmospheric Sciences, University of Nebraska-Lincoln, Lincoln, NE, USA, ²Department of Energy Resources Engineering, Stanford University, Stanford, CA, USA

Abstract Heat-pulse tracers are a promising field method to measure Darcy flux in the hyporheic zone. Interpretation of data collected from such tests typically assumes knowledge of the direction of local Darcy flux (vertical) and relies on simplified heat transport models with one-dimensional fluid flow and heat transfer. These assumptions are seldom valid due to complex flow geometry, heterogeneity, and the presence of localized heat sources. We derive a set of analytical expressions that obviate the need for these simplifying assumptions, thus substantially improving the capabilities of existing field instruments without requiring additional measurements. These closed-form solutions account for tensorial nature of heat-transfer parameters, and are obtained by using Green's functions and rotational coordinate transformations. The approach simplifies data collection, estimates three-dimensional Darcy flux, relates fluid flow to heat-transfer properties of the host medium, and can facilitate inverse modeling. Field applications of our solutions and their ramifications for data collection and analysis are discussed.

1. Introduction

Over the last decade, analyses of heat transfer in the hyporheic zone became an important tool for groundwater-surface water interaction studies. Such analyses are facilitated by the emergence of simple, miniaturized and computerized temperature measuring devices, which collect high-resolution data at low cost (Anderson, 2005; Constantz & Stonestrom, 2003; Rau et al., 2014).

The vast majority of experimental studies rely on two assumptions to interpret field data. First, the direction of one-dimensional (1D) flow is assumed to be known and fixed. Second, heat transport can be adequately described by the 1D analytical Suzuki-Stallman solution (Stallman, 1965; Suzuki, 1960). When stream temperature fluctuations have a strong vertical periodic component, analyses of its amplitude and phase yield information about the properties and 1D flow velocity. In fact, several recent studies found that such methods are prone to significant bias in locations with a pronounced horizontal velocity component (Angermann et al., 2013; Lautz, 2010; Rau et al., 2012; Reeves & Hatch, 2016; Roshan et al., 2012). However, hyporheic processes have substantial horizontal heat-transfer components that must be considered. While 1D and 2D analyses remain popular (e.g., Schneidewind et al., 2016), the 3D studies necessary in field work are more scarce (e.g., Boano et al., 2014) due to the complexity of flow geometry. This observation provided impetus for development of other heat-based tracer techniques, which offer significant advantages over natural thermal tracer tests.

Most of these techniques for characterization of multidimensional flow fields are performed using continuous steady heat sources and require significant experimental and computational resources. For example, a heavily instrumented and computationally intensive method of Ballard et al. (1996) allows one to characterize three-dimensional (3D) water flow and solute transport at a scale of about 1 m. A somewhat simpler experimental design of Labaky et al. (2007) relies on a two-dimensional (2D) flow assumption to infer plane flow at a scale about 0.1 m. These methods require drilling that may be very invasive.

Recently, substantial progress has been made in design of less invasive and more robust methods, whose support scale ranges from ~ 0.01 m (Yang et al., 2013) to ~ 0.1 m (Angermann et al., 2013; Lewandowski et al., 2011). Such spatial resolution is well suited for hyporheic flow characterization. These methods utilize heat sources of transient rate, and heat energy pulses on the order of 1 kJ, and offer a viable alternative to natural temperature tracer tests (Angermann et al., 2013; Lewandowski et al., 2011; Rau et al., 2012, 2014; Yang et al., 2013). A typical instrumental setup comprises a heat source and surrounding sensors that are

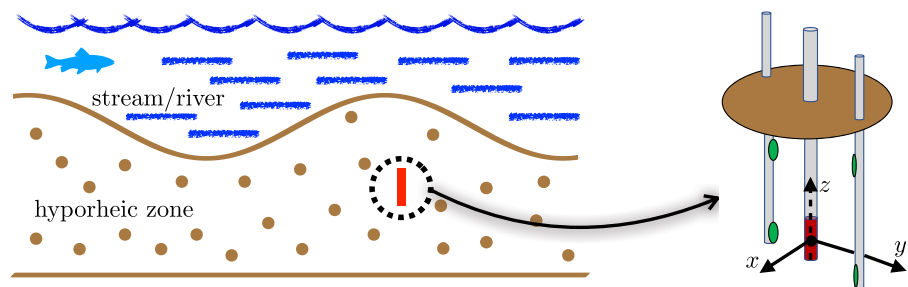


Figure 1. Left: Heat source embedded into the hyporheic zone beneath a stream. Right: Schematic representation of a heat-pulse sensor (after Angermann et al., 2013). The heat source (red) is surrounded by an array of temperature sensors (green). In the experimental setup of Angermann et al. (2013), the sensors are arranged in a circle with diameter 7 cm with vertical spacing of 3 cm between the sensors on the same rod.

inserted into a streambed in a regular cylindrical pattern, coaxial with the vertical line across the streambed (Figure 1). Short heat pulses as a heat tracer allow one to reduce a field experiment's time and to confine the spatial scale of averaging the Darcy flux measurements. The energy generated by a heat pulse from a point or linear source propagates in the subsurface by mechanisms of heat conduction, advection and dispersion; temperature measurements can be used to estimate Darcy flux. If Darcy flux varies both spatially and temporally, heat-pulse tracer tests are a viable alternative or a complement to natural heat-tracer tests that use temperature time series recorded by thermal sensors deployed in several observation points. One can expect heat pulse techniques obtain better estimates of multi-dimensional flows, whereas one-dimensional methods be better at obtaining time-series estimates.

Models used to interpret heat-pulse tracer tests lag behind developments in instrumentation, sensors, and digital data collection. That is because most, if not all, analytical models rely on a number of oversimplifying assumptions. For example, Yang et al. (2013) considered 2D heat transfer in a fixed flow plane, whose orientation must be known a priori; this is seldom the case in hyporheic studies. In addition, they entirely ignore heat dispersion. Other models do consider heat dispersion but ignore heat conduction (e.g., Lewandowski et al. [2011, p. 3252]; and Angermann et al. [2013]). Ad hoc procedures for estimation of the magnitude and direction of Darcy flux, which have no hydrodynamic basis, yield dispersivity values that are inconsistent with established trends (Angermann et al., 2013, Figure 8) and cannot be extended to other instrument configurations. That indicates a need for new heat-transfer models, which would lead to more robust field data interpretation.

Despite its current shortcomings, the transient heat-pulse approach is promising because it relies on existing field instrumentation (e.g., developed by Lewandowski et al., 2011) and yields data adequate for 3D interpretation. With proper interpretation methods, it also eliminates a need for reinsertion of instruments into the subsurface. Rather than using numerical codes, e.g., VS2D and COMSOL (Constantz & Stonestrom, 2003; Reeves & Hatch, 2016), we posit that more efficient analytical tools are essential for data interpretation, especially in the context of inverse modeling.

Our analysis of heat transfer in the hyporheic zone provides tools for estimation of Darcy flux with arbitrary orientation in three dimensions. The modeling tools account for heat dispersion, flexible source type (point or distributed), and heat-pulses of finite duration and heat-pulses with periodicity components. The latter capability may provide an effective strategy for delineation of the test scale. The versatility of our analytical model maximizes the information content of both existing data sets and measurements that can be collected with existing instrumentation without modification of field procedures. Although stimulated by hyporheic zone studies in stream-aquifer interactions, our solutions are broadly applicable to chemical tracers.

2. Problem Formulation

Even in homogeneous and isotropic soils, thermal conductivity κ is a positive-definite second-rank tensor and heat transfer is described by a convection-dispersion equation (Anderson, 2005; Bear, 1972; Ciriello et al., 2015; Ingebritsen et al., 2006)

$$\rho c \frac{\partial T}{\partial t} = \nabla \cdot (\boldsymbol{\kappa} \nabla T) - \rho_w c_w \mathbf{q} \cdot \nabla T + F. \quad (1)$$

Here $T(\mathbf{x}, t)$ is temperature of the medium at point $\mathbf{x} = (x, y, z)^T$ and time t ; ρ_w and c_w are the density and specific heat capacity of water, respectively; the heat capacity ρc is calculated by a mixing rule (e.g., Bear, 1972) such that

$$\rho c = n \rho_w c_w + (1-n) \rho_s c_s, \quad (2)$$

where n is porosity, and ρ_s and c_s are the density and heat capacity of hosting medium (solids); $F(\mathbf{x}, t)$ is a prescribed source of heat; and $\mathbf{q} = (q_x, q_y, q_z)^T = -K \nabla h$ is the Darcy flux vector, with K and h denoting hydraulic conductivity and hydraulic head, respectively. To simplify the subsequent presentation, we recast (1) as

$$\frac{\partial T}{\partial t} = \nabla \cdot (\mathbf{D} \nabla T) - \mathbf{V} \cdot \nabla T + f. \quad (3a)$$

where

$$\mathbf{D} = \frac{\boldsymbol{\kappa}}{\rho c}, \quad \mathbf{V} = \frac{\rho_w c_w}{\rho c} \mathbf{q}, \quad f = \frac{F}{\rho c}. \quad (3b)$$

For thermally isotropic aquifers, the thermal dispersion tensor \mathbf{D} is completely characterized by two dispersivity parameters, α_L and α_T (e.g., equation (10.4.17) in Bear [1972], equation (5) in Burnett & Frind [1987], p. 46 of Zheng & Bennett [2002], and equation (26) in Lichtner et al. [2002]). These parameters have dimensions of length (Bear, 1972; Ingebritsen et al., 2006) and must be obtained experimentally.

2.1. Thermal Conductivity Tensor

In the absence of flow, the thermal conductivity of a water-saturated medium is a scalar κ_0 related to the thermal conductivities of water (κ_w) and solids (κ_s) by (e.g., Ingebritsen et al., 2006, p. 134)

$$\kappa_0 = \kappa_w^{1-n} \kappa_s^n, \quad \text{so that} \quad D_0 = \frac{\kappa_0}{\rho c}. \quad (4)$$

The units and typical values of these and other thermal properties of water and solids are listed in Table 1. The tensorial nature of the thermal conductivity $\boldsymbol{\kappa}$ or thermal dispersion \mathbf{D} stems from both convection and dispersion. Unlike its mass transport counterparts (the hydrodynamic dispersion tensor), the thermal conductivity tensor is much less studied experimentally (Bear, 1972; Gelhar et al., 1992; Rau et al., 2014), and relatively little information is available about anisotropy of the thermal properties. A few analyses of field studies of subsurface heat transfer suggest that thermal conductivity is indeed a tensor (e.g., Anderson [2005] and de Marsily [1986, p. 279]). Following Rau et al. (2012) and Bons et al. (2013), we assume a linear dependence of these tensor parameters on magnitude of the Darcy flux. This assumption is widely used in the context of subsurface solute transport (Zheng & Bennett, 2002), although there are some indications that, under certain conditions, heat dispersion might follow a power law (rather than linear) relation (Bons et al., 2013; Rau et al., 2012).

Parameterization of \mathbf{D} is far from straightforward and must account for a number of factors. First, dispersive processes in water-saturated geologic materials are often deemed to be less significant for heat transfer than for solute transport, because the thermal conductivity of solid matrix exceeds that of water by more than an order of magnitude (e.g., Bear [1972, p. 651]; and de Marsily [1986]) and the role of water in creating dispersion effects is often neglected (Coutelieris & Delgado, 2012; Yang et al., 2013). Second, a scale effect in thermal anisotropy may be expected, similar to that observed for mass-transport processes (e.g., Gelhar et al., 1992; Zech et al., 2015). We adopt a general ("classical") parametrization of the thermal dispersion tensor for isotropic media (e.g., Bear [1972], equation (10.4.17); Burnett & Frind [1987], equation (5); Zheng & Bennett [2002, p. 46]; and Lichtner et al. [2002], equation (26)). The tensor depends on material

Table 1
Values of Thermal Properties of Water and Solids Used in Our Simulations (After Reeves & Hatch [2016] and Irvine et al. [2015])

Parameter	Units	Value
specific heat capacity of water, c_w	J/(kg°K)	4184
specific heat capacity of solids, c_s	J/(kg°K)	800
density of water, ρ_w	kg/m ³	998
density of solids, ρ_s	kg/m ³	2650
thermal conductivity of water, κ_w	W/(m°K)	0.6
thermal conductivity of solids, κ_s	W/(m°K)	8.4 ^a

^aAlternatively, if volumetric fraction (n_q) of quartz in a mixture is known, then one can compute thermal conductivity of solids from a relation (Farouki, 1986) $\kappa_s = \kappa_{s,q}^{n_q} \kappa_{s,nq}^{(1-n_q)}$, where $\kappa_{s,q}$ and $\kappa_{s,nq}$ are the thermal conductivities of quartz and non-quartz components in a mixture, respectively.

Table 2
Values of Hydrodynamic and Transport Parameters Used in Our Simulations

Parameter	Units	Value
Darcy flux, q	m/s	10^{-6} or 10^{-5}
polar angle, ϕ	rad	$0 \leq \phi < 2\pi$
azimuthal angle, θ	rad	$0 \leq \theta < \pi$
porosity, n	–	0.3
longitudinal thermal dispersivity, α_L	m	0.2 ^a
transverse thermal dispersivity, α_T	m	0.05
heat-pulse energy, E	J	2000

^aThe value of Darcy flux q is consistent with those reported by (Ong & Zlotnik, 2011, Table 2) and (Angermann et al., 2013, Figure 7), and the value of longitudinal dispersivity α_L with those from (Angermann et al., 2013, Figure 8).

properties and Darcy flux characteristics; guided by the observations reported in Figure 8 of Angermann et al. (2013) for the experimental setup described by our model, we assign to the principal components of this tensor values reported in Table 2. These values are used for illustrative purposes only. Our analytical solutions can also accommodate pure heat conduction by setting the dispersivity coefficients to 0, if data interpretation suggests small or negligible contribution of heat dispersion. We use non-zero values for the dispersivity coefficients because (Rau et al., 2014, p. 45) “thermal dispersion can be of significance and its role should be investigated further to give a better basis for heat transport calculations in applications relating to sediment heat tracing” (see, also, [Bons et al., 2013, p. 6176]).

2.2. Field and Principal Coordinate Systems

Registration of locations of heaters and sensors is naturally performed in a field-based Cartesian coordinates system, whose z axis points

upward. Since the Darcy flux vector is, in general, not aligned with the vertical direction, this results in the thermal conductivity being a full tensor. General properties of tensors suggest the existence of a principal coordinate system $(\tilde{x}, \tilde{y}, \tilde{z})$ in which all the off-diagonal components of the thermal dispersivity tensor \mathbf{D} are zero. This coordinate system is obtained by aligning the \tilde{z} coordinate with the flow direction, so that $\mathbf{q} = (0, 0, q)^T$. In this coordinate system, the thermal dispersivity tensor \mathbf{D} takes the form

$$\mathbf{D} = \begin{pmatrix} D_T & 0 & 0 \\ 0 & D_T & 0 \\ 0 & 0 & D_L \end{pmatrix}, \quad D_T \equiv \frac{\kappa_T}{\rho c} = D_0 + \alpha_T V, \quad D_L \equiv \frac{\kappa_L}{\rho c} = D_0 + \alpha_L V, \quad V = \frac{\rho_w c_w}{\rho c} q, \quad (5)$$

and the general form of heat transfer equation (1) simplifies to

$$\frac{\partial T}{\partial t} = D_T \left(\frac{\partial^2 T}{\partial \tilde{x}^2} + \frac{\partial^2 T}{\partial \tilde{y}^2} \right) + D_L \frac{\partial^2 T}{\partial \tilde{z}^2} - V \frac{\partial T}{\partial \tilde{z}} + f. \quad (6)$$

This equation is easier to solve analytically than its counterpart (1) (e.g., Cardiff et al., 2010; Zlotnik et al., 2017). To find the temperature distribution in the field system, one needs to establish a relationship between these two systems. A transformation of the field coordinates system (x, y, z) into the principal coordinates system $(\tilde{x}, \tilde{y}, \tilde{z})$ is accomplished by rotation (Appendix A)

$$\begin{pmatrix} \tilde{x} \\ \tilde{y} \\ \tilde{z} \end{pmatrix} = \begin{pmatrix} \cos \theta (x \cos \phi + y \sin \phi) - z \sin \theta \\ -x \sin \phi + y \cos \phi \\ \sin \theta (x \cos \phi + y \sin \phi) + z \cos \theta \end{pmatrix}. \quad (7)$$

Angles ϕ and θ characterize the direction of Darcy flux \mathbf{q} in the field coordinate system (x, y, z) , as shown in Figure 2. Unfortunately, they are not known a priori and have to be inferred from field data together with values of q , α_L , and α_T . We assume that values of the remaining parameters, n , $\rho_w c_w$, and κ_i (with $i=w$ and s), are known (see Table 2), and that (2) and (4) or similar constitutive relationships provide adequate estimates of ρc and κ_0 .

3. Analytical Solutions for Different Heat Sources

We use Green’s functions to develop analytical solutions for point and line sources that are either constant in time or emit periodic signals. Since heat-pulse methods affect a relatively small volume near the heat source (Figure 1), we treat the subsurface environment as infinite. For a 3D infinite domain, the Green’s function $\mathcal{G}(\tilde{x} - \xi_1, \tilde{y} - \xi_2, \tilde{z} - \xi_3, t - \tau)$ represents the temperature response at point $(\tilde{x}, \tilde{y}, \tilde{z})$ and time t to an instantaneous point source of infinite strength located at space-time point $(\xi_1, \xi_2, \xi_3, \tau)$. It satisfies (6) with $f \equiv \delta(\tilde{x} - \xi_1) \delta(\tilde{y} - \xi_2) \delta(\tilde{z} - \xi_3) \delta(t - \tau)$, where $\delta(\cdot)$ is the Dirac delta function, and is subject to the zero initial condition and zero boundary condition at infinity. Its explicit form is given by (e.g., Hunt, 1978; Park & Zhan, 2001)

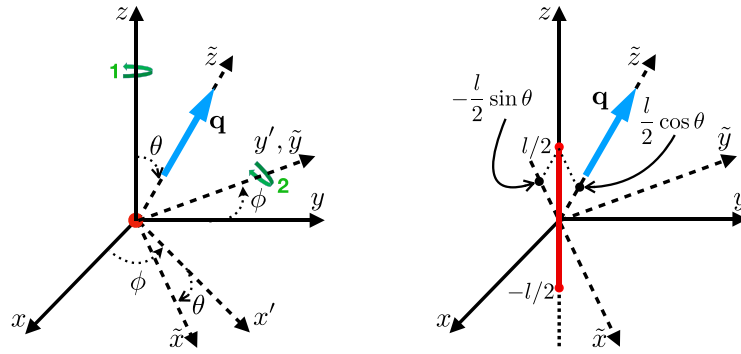


Figure 2. Left: Field (solid lines) and principal (dashed lines) orthogonal coordinate systems (x, y, z) and $(\tilde{x}, \tilde{y}, \tilde{z})$, respectively. The \tilde{z} coordinate of the transformed (principal) coordinate system is aligned with the direction of Darcy flux \mathbf{q} (blue vector). The transformation $(x, y, z) \rightarrow (\tilde{x}, \tilde{y}, \tilde{z})$ is accomplished via two rotations. Counterclockwise rotation 1, around the z axis by angle ϕ , transforms (x, y, z) into an intermediate coordinate system (x', y', z) . Counterclockwise rotation 2, around the y' axis by angle θ , aligns the new z' axis with vector \mathbf{q} . Note that axes \tilde{x} , \tilde{z} , and z are located in one plane. A point heat-source is located in the origin of the coordinate system (red dot). Right: A vertical line heat-source (solid red line) of length l , distributed along the z axis of the field coordinates system (x, y, z) between $z = -l/2$ and $z = l/2$. In the principal coordinate system $(\tilde{x}, \tilde{y}, \tilde{z})$, this source is represented by a line connecting points $(-l/2 \sin \theta, 0, l/2 \cos \theta)$ and $(l/2 \sin \theta, 0, -l/2 \cos \theta)$.

$$G = \frac{1}{8\pi^{3/2} \sqrt{D_L D_T^2} (t-\tau)^{3/2}} \exp \left[-\frac{(\tilde{x} - \xi_1)^2 + (\tilde{y} - \xi_2)^2}{4D_T(t-\tau)} - \frac{(\tilde{z} - \xi_3 - V(t-\tau))^2}{4D_L(t-\tau)} \right]. \quad (8)$$

For any source function with finite support, $f(\tilde{x}, \tilde{y}, \tilde{z}, t)$, the solution of (6) is

$$T(\tilde{x}, \tilde{y}, \tilde{z}, t) = \int_0^t \int_{-\infty}^{\infty} \int_{-\infty}^{\infty} \int_{-\infty}^{\infty} f(\xi_1, \xi_2, \xi_3, \tau) G(\tilde{x} - \xi_1, \tilde{y} - \xi_2, \tilde{z} - \xi_3, t - \tau) d\xi_1 d\xi_2 d\xi_3 d\tau, \quad (9)$$

where T describes the temperature increase (in $^{\circ}\text{C}$) over the initial spatially uniform temperature.

3.1. Instantaneous Point Source

An instantaneous (at time $t = 0$) point source that is located at the coordinates origin is represented by $f = E / (\rho c) \delta(\tilde{x}) \delta(\tilde{y}) \delta(\tilde{z}) \delta(t)$ where E is heat-pulse energy. Substituting this expression into (9) yields a temperature distribution induced by an instantaneous point source,

$$T = \frac{E / (\rho c)}{8\pi^{3/2} \sqrt{D_L D_T} t^{3/2}} \exp \left[-\frac{\tilde{x}^2 + \tilde{y}^2}{4D_T t} - \frac{(\tilde{z} - Vt)^2}{4D_L t} \right]. \quad (10)$$

A similar solution for solute transport can be found in Hunt (1978) and (Ingebritsen et al., 2006, equation (3.23)), among others. The corresponding temperature distribution in the field coordinate system (x, y, z) is obtained by combining this solution with (7). Figure 3 illustrates properties of a thermal signal in the vicinity of an instantaneous point-source heat-pulse heater in the presence of the upward Darcy flux q_z ($\phi = \theta = 0$). The isotherms of the snapshot of $T(x, y = 0, z, t = 1000 \text{ s})$ (Figure 3, Left) exhibit cross-sections (in the plane $y = 0$) of rotational ellipsoids whose centers are slightly shifted in the velocity direction from the heat source located at $\mathbf{x} = \mathbf{0}$. The temperature dynamics at two sensor locations \mathbf{x}^* are shown in Figure 3 (Right) for Darcy velocities $q_z = 10^{-6} \text{ m/s}$ and 10^{-5} m/s . These curves reveal the maximal temperature to be on the order of 1°C , which is acceptable for data collection and interpretation. If needed, longer pulses or a greater pulse energy can be used.

3.2. Finite-Duration Pulse From Point Source

Heat-pulse instruments may generate a heat pulse, E , over a finite time period t_p . For uniform heat production rate E/t_p over this time period, $f = E / (\rho c t_p) \delta(\tilde{x}) \delta(\tilde{y}) \delta(\tilde{z}) g(t)$ with $g \equiv 1$ for $0 < t \leq t_p$ and $g \equiv 0$ otherwise. For this source term, (9) yields a temperature distribution induced by a point source of finite duration,

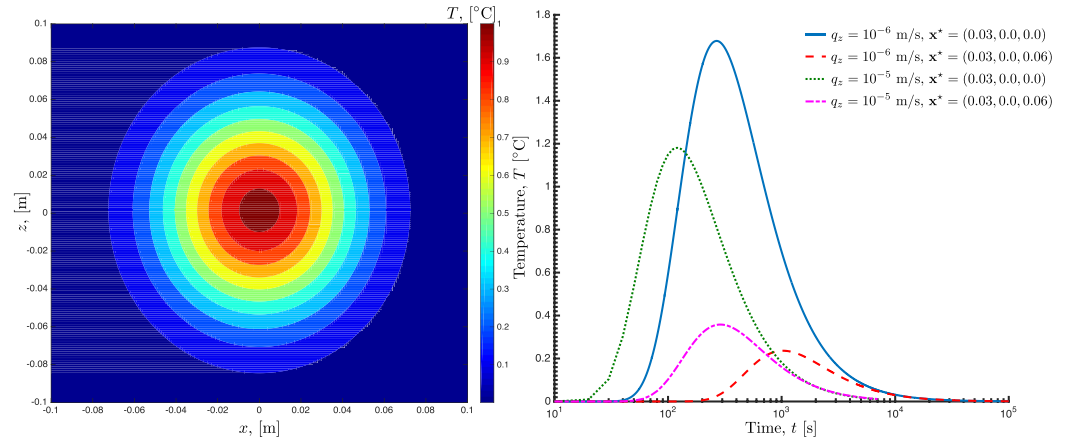


Figure 3. Temperature T in the vicinity of an instantaneous point-source heat-pulse heater in the presence of the upward Darcy flux q_z ($\phi = \theta = 0$). Left: a snapshot, at $t = 1000$ s, of the temperature T in the $y = 0$ cross-section. Right: Temperature dynamics at two sensor locations $\mathbf{x}^* = (0.03 \text{ m}, 0.0 \text{ m}, 0.0 \text{ m})$ and $\mathbf{x}^* = (0.03 \text{ m}, 0.0 \text{ m}, 0.06 \text{ m})$, shown for Darcy velocities $q_z = 10^{-6} \text{ m/s}$ and 10^{-5} m/s .

$$T(\tilde{x}, \tilde{y}, \tilde{z}, t) = \begin{cases} T_p(\tilde{x}, \tilde{y}, \tilde{z}, t) & 0 \leq t \leq t_p \\ T_p(\tilde{x}, \tilde{y}, \tilde{z}, t) - T_p(\tilde{x}, \tilde{y}, \tilde{z}, t - t_p) & t \geq t_p \end{cases} \quad (11a)$$

where

$$T_p(\tilde{x}, \tilde{y}, \tilde{z}, t) = \frac{E/(\rho c)}{8\pi D_T t_p R} e^{-\tilde{R}} \operatorname{erfc}\left(\frac{R-Vt}{2\sqrt{D_L t}}\right) + e^{\tilde{R}} \operatorname{erfc}\left(\frac{R+Vt}{2\sqrt{D_L t}}\right) \quad (11b)$$

with

$$R = \sqrt{\frac{D_L}{D_T}(\tilde{x}^2 + \tilde{y}^2) + \tilde{z}^2}, \quad \tilde{z} = \frac{\tilde{z}V}{2D_L}, \quad \tilde{R} = \frac{RV}{2D_L} \quad (11c)$$

In the context of solute transport and for source of infinite duration ($t_p \rightarrow \infty$, i.e., $T = T_p$) a solution similar to (11b) was developed by Hunt (1978).

3.3. Instantaneous Line Source

Consider, next, the total instantaneous heat pulse $E/(\rho c)$ that is uniformly distributed over length l in the vertical direction (Figure 2), rather than being concentrated at a point. In the field coordinate system (x, y, z) , this setting is represented by the source term $f(x, y, z, t) = E/(\rho c l) g(z) \delta(x) \delta(y) \delta(t)$ with $g \equiv 1$ for $|z| \leq l$ and $g \equiv 0$ otherwise. In the principal coordinate system $(\tilde{x}, \tilde{y}, \tilde{z})$ this translates into (e.g., Zhan & Zlotnik, 2002) $f(\tilde{x}, \tilde{y}, \tilde{z}, t) = E/(\rho c l) g(\tilde{x}) \delta(\tilde{x} \cos \theta + \tilde{z} \sin \theta) \delta(\tilde{y}) \delta(t)$ with $g \equiv 1$ for $|\tilde{x}| \leq (l/2) \sin \theta$ and $g \equiv 0$ otherwise. Substituting this expression into (9) yields a temperature distribution induced by an instantaneous line source (Appendix B),

$$T = \frac{E/(l\rho c)}{8\pi\gamma D_T t} \exp\left[-\frac{\tilde{x}^2 + \tilde{y}^2}{4D_T t} - \frac{(\tilde{z} - Vt)^2}{4D_L t} + \frac{\beta^2}{\alpha}\right] [\operatorname{erf}(\eta_+) - \operatorname{erf}(\eta_-)], \quad (12a)$$

where $\eta_{\pm} = \pm(l\sqrt{\alpha}/2)\sin\theta - \beta/\sqrt{\alpha}$ and

$$\alpha = \frac{1}{4D_T t} + \frac{\cot^2\theta}{4D_L t}, \quad \beta = \frac{\tilde{x}}{4D_T t} - \frac{(\tilde{z} - Vt)\cot\theta}{4D_L t}, \quad \gamma = \sqrt{(D_L/D_T)\sin^2\theta + \cos^2\theta}. \quad (12b)$$

Note that $\lim_{\theta \rightarrow 0} \beta/\sqrt{\alpha} = (\tilde{z} - Vt)/\sqrt{4D_L t}$.

3.4. Periodic Point Source

Effects of periodic fluctuations of a heater's output diminish rapidly with distance from sensors to a heater; this effect is also accompanied by a sensor's phase shift (Stallman, 1965; Suzuki, 1960). Consequently, such an experimental setup can be used to characterize a finite volume in the immediate vicinity of a heater by

adding a periodic component to the constant rate of heat production, as was done by Cardiff et al. (2013) to analyze pressure fluctuations. A temperature field generated by the constant-rate heat production is described by (11b). A periodic point-source of heat is represented by $f = E_\omega / (\rho c) \sin(\omega t) \delta(\tilde{x}) \delta(\tilde{y}) \delta(\tilde{z})$, where ω [1/s] and E_ω [W] are the angular frequency and amplitude of heat production fluctuations, respectively. Substituting this expression into (9) yields a correction to the temperature distribution from constant-rate heating superposed with a periodic point-source (Appendix B),

$$T = \frac{E_\omega / (\rho c)}{8\pi^{3/2} \sqrt{D_L D_T}} [\mathcal{I}_1(\tilde{x}, \tilde{y}, \tilde{z}, t) \sin(\omega t) - \mathcal{I}_2(\tilde{x}, \tilde{y}, \tilde{z}, t) \cos(\omega t)], \quad (13a)$$

where

$$\begin{aligned} \mathcal{I}_1 &= \int_0^t \frac{\cos(\omega\tau)}{\tau^{3/2}} \exp\left[-\frac{\tilde{x}^2 + \tilde{y}^2}{4D_T\tau} - \frac{(\tilde{z} - V\tau)^2}{4D_L\tau}\right] d\tau, \\ \mathcal{I}_2 &= \int_0^t \frac{\sin(\omega\tau)}{\tau^{3/2}} \exp\left[-\frac{\tilde{x}^2 + \tilde{y}^2}{4D_T\tau} - \frac{(\tilde{z} - V\tau)^2}{4D_L\tau}\right] d\tau. \end{aligned} \quad (13b)$$

For large t , this solution gives rise to an asymptotic expression

$$T = \frac{E_\omega / (\rho c)}{8\pi^{3/2} \sqrt{D_L D_T}} \sqrt{l_1^2 + l_2^2} \sin[\omega t - \arctan(l_1/l_2)], \quad (14)$$

where $l_i(\tilde{x}, \tilde{y}, \tilde{z}) = \mathcal{I}_i(\tilde{x}, \tilde{y}, \tilde{z}, \infty)$ with $i = 1, 2$. Therefore, temperature oscillations of the source and an observation point are generally out of phase. The temperature phase shift in observation point depends on location and transport parameters. The amplitude and phase shifts are defined by integrals l_1 and l_2 : the amplitude, $\sqrt{l_1^2 + l_2^2}$, decreases with distance from the source, while the phase shift characteristic, l_1/l_2 varies from 0 to π . Phase and attenuation analyses can be used for simplified evaluation of the heat transport properties. This approach generalizes existing methods that require sensor placement on a vertical line (Lautz, 2010).

4. Inference of Flow Fields From Heat Tracer Experiments

All heat tracer-based methods start by establishing a field system of Cartesian coordinates in which the z coordinate is commonly oriented vertically (Hatch et al., 2006; Lewandowski et al., 2011; Reeves & Hatch, 2016, etc). The next step is to register coordinates of an i th sensor, (x_i^*, y_i^*, z_i^*) with $i = 1, \dots, N$ where N denotes the number of sensors. In heat-pulse tests with a fixed configuration of a heater and probes, Lewandowski et al. (2011) and Angermann et al. (2013) deploy the heater at a depth less than 0.5 m, and arrange the probes in 4 circles of 7 cm diameter ($N = 16$ or 24). Yang et al. (2013) use a heater and sensors arranged in a circle of diameter about 1.3 cm ($N = 4$).

When an artificial heat source is used, its size (length) must be compared with the distance to the nearest sensor. If the source size is small, one can use a point source model (10), otherwise the linear source model (12) should be deployed. These solutions provide temperature distributions in a principal system of coordinates. Equation (7) is used to transform these solutions to a field coordinate system for comparison with field data from each of the N sensors. Figure 4 exhibits temperature response, $T(\mathbf{x}^*, t)$, recorded by a sensor at point $(x^* = 0.03 \text{ m}, y^* = 0.0 \text{ m}, z^* = 0.03 \text{ m})$ to the instantaneous point source at $(x = 0.0 \text{ m}, y = 0.0 \text{ m}, z = 0.0 \text{ m})$, as predicted by (10) for three values of θ .

To ascertain the method's sensitivity, the maximum temperatures reached at observation points (T_{\max}) are needed. Figure 5 demonstrates how strongly T_{\max} can be affected by the direction of the 3D velocity \mathbf{V} . For each sensor, T_{\max} for the upward-oriented velocity ($\theta = 0$) is different from that for the downward-oriented velocity ($\theta = \pi$) due to the sensor position relative to the heater.

Heat pulses may have substantial duration compared to observation time. For example, Yang et al. (2013) used a 9 s pulse and measurement time of 120 s, while Angermann et al. (2013) used a 60 s pulse and measurement time of 800 s. Corresponding errors in the test methods can be assessed with (11).

All equations in the principal system of coordinates contain two unknown media characteristics (α_L and α_D) and the magnitude of heat-transport velocity, V . The heat-transport velocity vector in the field system of coordinates, $\mathbf{V} = (V_x, V_y, V_z)^T$, also includes rotation angles ϕ and θ such that

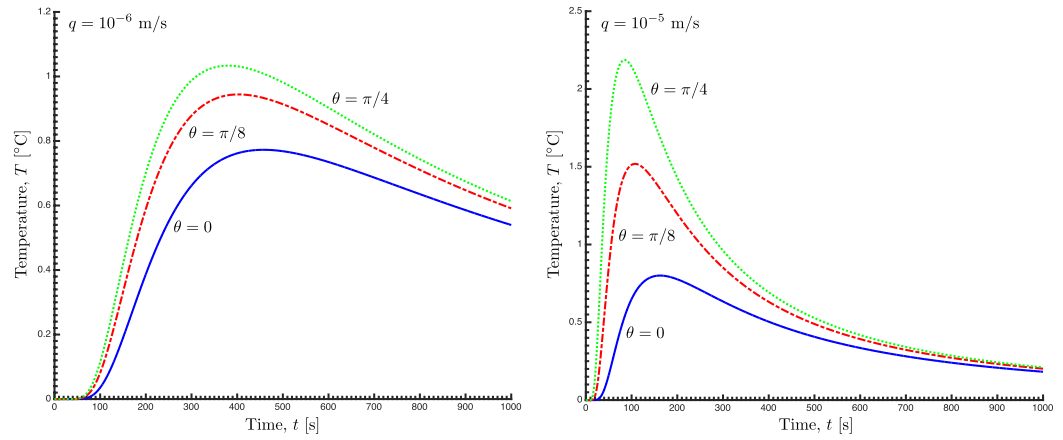


Figure 4. Temperature response at point $(x^*=0.03 \text{ m}, y^*=0.0 \text{ m}, z^*=0.03 \text{ m})$ to the instantaneous point source at $(x=0.0 \text{ m}, y=0.0 \text{ m}, z=0.0 \text{ m})$, as predicted by (10) for Darcy flux $q=10^{-6} \text{ m/s}$ and 10^{-5} m/s with azimuthal angle $\theta = 0, \pi/8$ and $\pi/4$.

$$\mathbf{V} = V \begin{pmatrix} \sin \theta \cos \phi \\ \sin \theta \sin \phi \\ \cos \theta \end{pmatrix}. \quad (15)$$

Finally, the Darcy flux in the field coordinates is obtained using relationship

$$\mathbf{q} = \frac{\rho C}{\rho_w C_w} \mathbf{V}. \quad (16)$$

These five parameters ($\alpha_L, \alpha_T, V, \theta$, and ϕ) can be inferred from data via inverse modeling. Equations (10), (12), and (13a) contain other parameters: $E, \rho C$ and κ_0 when heat dispersion is neglected (e.g., Ingebritsen et al., 2006; Yang et al., 2013), or parameters $E, \rho C, \kappa_L$, and α_T when it is considered (Angermann et al., 2013; Reeves & Hatch, 2016).

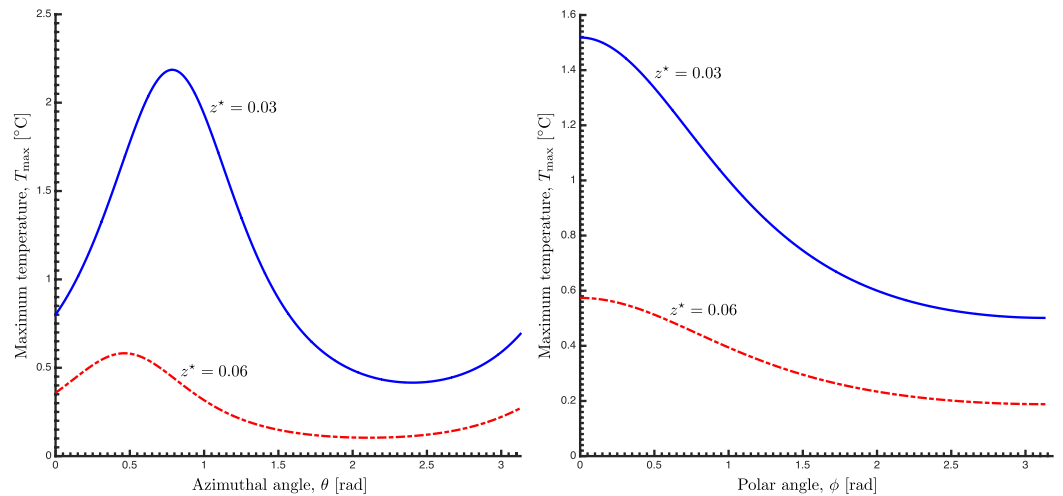


Figure 5. Maximum temperature $T_{\max} = \max_t T(\mathbf{x}, t)$ at points $(x^*=0.03 \text{ m}, y^*=0.0 \text{ m}, z^*=0.03 \text{ m})$ and $(x^*=0.03 \text{ m}, y^*=0.0 \text{ m}, z^*=0.06 \text{ m})$ generated by the instantaneous point source at $(x=0.0 \text{ m}, y=0.0 \text{ m}, z=0.0 \text{ m})$, as predicted by (10) for Darcy flux $q=10^{-5} \text{ m/s}$ and (left) azimuthal angle $0 \leq \theta \leq \pi$ and polar angle $\phi=0.0$ or (right) azimuthal angle $\theta=\pi/8$ and polar angle $0 \leq \phi \leq \pi$.

In some cases, especially for simplified treatment of 1D or 2D velocity, a smaller number of parameters than 5 can be searched: only 3 parameters (α_L , α_D , V_z) in the case of (Angermann et al., 2013, p. 3), and only two parameters (V_x and V_y) in the case of (Yang et al., 2013, p. 5883). Therefore, other parameters could be included into the list of searched ones (e.g., E in case of Angermann et al. [2013]), or κ_0 and ρc (e.g., Yang et al., 2013). In the general case, independent parameters E , n , ρ_s , c_s and κ_s , which are unrelated to dispersive heat transport, should be estimated a priori from laboratory measurements, site-specific data from other tests, or constitutive relationships such as (2) and (4) for estimating ρc and κ_0 ; water characteristics ρ_w , c_w , and κ_w are known constants.

Our solutions provide the most complete description of heat dispersion and transport dimensionality to date. Previous treatments of thermal conductivity are inconsistent between approaches. For example, Yang et al. (2013) ignore dispersion entirely, and their 2D method requires rearrangement of field settings if 3D Darcy velocity has to be found. While omission of heat dispersion is common (e.g., Ingebritsen et al., 2006), validation of such an approach requires further analyses (Anderson, 2005; Bons et al., 2013; de Marsily, 1986; Rau et al., 2014). The method of Angermann et al. (2013) accounts for heat dispersion but ignores heat conduction, and uses ad hoc coordinate conversions of the 3D temperature field. As a result, such interpretation leads to unphysical estimates of the dispersivity that should decrease with velocity magnitude (Lewandowski et al., 2011, Figure 8). Yet, the novel instrumentation used in these studies offers new opportunities to study heat dispersion in the field.

5. Conclusions

Previous interpretations of heat-pulse methods constrained the search for the Darcy flux vector to one or two components. The proposed analytical approach to analysis of temperature distributions from heat-pulse tracer tests enables one to use the recently developed instrumentation (Angermann et al., 2013; Lewandowski et al., 2011; Yang et al., 2013, and references therein) to interpret already available data and extract maximum information from new tests in 3D.

Less dense placement of the heat probe and sensors can be used, thereby providing more options for data collection (larger spacing, irregular grid of sensors, greater and easier insertion depths by individual sensors, and changing velocity measurement scale). Limiting repeated sensor insertions into the subsurface ameliorates media disturbance and noise from data interpretation.

On the other hand, by relating the support volume of a heat probe to both its operation regime and thermal and hydraulic properties of the surrounding sediments, our solutions can be used to determine the maximal spacing between the probe and sensors.

In previous studies, heat sources were usually highly idealized: they were assumed to be instantaneous and focused in a point. Our solution allows for a real-size heater (a linear segment) of a length that is comparable to distances between the heater and surrounding sensors.

Digitally operated heaters allow for control of the heat production rate, imposing, e.g., periodic, fixed-rate and pulsed-amplitude, and other regimes. By facilitating accurate and rapid measurements, our theory may provide new opportunities to study heat transport in homogeneous and heterogeneous media, when numerous local-scale measurements are needed.

Appendix A: Coordinate Transformation

The transformation of coordinates is performed in two rotations using Euler's angles. Following (Boas, 2006, p. 129), we first rotate the (x, y, z) coordinate system around the z axis by an angle ϕ , and then around the \bar{y} axis by an angle θ (Figure 2). The first rotation transforms the (x, y, z) coordinate system into an intermediate system of coordinates (x', y', z) , such that

$$\begin{pmatrix} x' \\ y' \\ z \end{pmatrix} = \begin{pmatrix} \cos \phi & \sin \phi & 0 \\ -\sin \phi & \cos \phi & 0 \\ 0 & 0 & 1 \end{pmatrix} \begin{pmatrix} x \\ y \\ z \end{pmatrix} = \begin{pmatrix} x \cos \phi + y \sin \phi \\ -x \sin \phi + y \cos \phi \\ z \end{pmatrix}. \quad (\text{A.1})$$

After this rotation, the y' component of vector \mathbf{q} becomes 0, but its x' -component remains, in general, non-zero.

The second rotation, around the y' axis by angle θ , is related to the new left system of coordinates (Boas, 2006, p. 129). It aligns the new \tilde{z} axis with the direction of \mathbf{q} , so that in this new coordinate system $\mathbf{q}=(0, 0, q)^\top$. This rotation transforms the (x', y', z) coordinate system into the $(\tilde{x}, \tilde{y}, \tilde{z})$ coordinate system according to

$$\begin{pmatrix} \tilde{x} \\ \tilde{y} \\ \tilde{z} \end{pmatrix} = \begin{pmatrix} \cos \theta & 0 & -\sin \theta \\ 0 & 1 & 0 \\ \sin \theta & 0 & \cos \theta \end{pmatrix} \begin{pmatrix} x' \\ y' \\ z \end{pmatrix}. \quad (\text{A.2})$$

Combining (A.1) and (A.2) yields (7).

Appendix B: Derivation of Analytical Solutions

B1. Instantaneous Line Source

Combining (8) and (9) with $f(\tilde{x}, \tilde{y}, \tilde{z}, t)=E/(\rho cl)g(\tilde{x})\delta(\tilde{x}\cos\theta+\tilde{z}\sin\theta)\delta(\tilde{y})\delta(t)$ yields

$$\begin{aligned} T &= \frac{E}{\rho cl} \int_{-\infty}^{\infty} \int_{-(l/2)\sin\theta}^{(l/2)\sin\theta} \delta(\xi_1 \cos \theta + \xi_3 \sin \theta) \mathcal{G}(\tilde{x} - \xi_1, \tilde{y}, \tilde{z} - \xi_3, t) d\xi_1 d\xi_3 \\ &= A \int_{-\infty}^{\infty} \int_{-(l/2)\sin\theta}^{(l/2)\sin\theta} \delta(\xi_1 \cos \theta + \xi_3 \sin \theta) \exp \left[-\frac{(\tilde{x} - \xi_1)^2 + \tilde{y}^2}{4D_T t} - \frac{(\tilde{z} - \xi_3 - Vt)^2}{4D_L t} \right] d\xi_1 d\xi_3 \end{aligned} \quad (\text{B.1a})$$

where

$$A = \frac{E}{\rho cl} \frac{1}{8\pi^{3/2} \sqrt{D_L D_T t^{3/2}}}. \quad (\text{B.1b})$$

Using basic properties of the delta function, we obtain

$$T = \frac{A}{\sin \theta} \int_{-(l/2)\sin\theta}^{(l/2)\sin\theta} \exp \left[-\frac{(\tilde{x} - \xi_1)^2 + \tilde{y}^2}{4D_T t} - \frac{(\tilde{z} + \xi_1 \cot \theta - Vt)^2}{4D_L t} \right] d\xi_1, \quad (\text{B.2})$$

which, after some algebraic manipulations, gives rise to

$$T = A_1 \int_{-(l/2)\sin\theta}^{(l/2)\sin\theta} \exp \left[-\left(\frac{1}{4D_T t} + \frac{\cot^2 \theta}{4D_L t} \right) \xi_1^2 + 2 \left(\frac{\tilde{x}}{4D_T t} - \frac{(\tilde{z} - Vt) \cot \theta}{4D_L t} \right) \xi_1 \right] d\xi_1, \quad (\text{B.3a})$$

where

$$A_1 = \frac{E}{\rho cl \sin \theta} \frac{1}{8\pi^{3/2} \sqrt{D_L D_T t^{3/2}}} \exp \left[-\frac{\tilde{x}^2 + \tilde{y}^2}{4D_T t} - \frac{(\tilde{z} - Vt)^2}{4D_L t} \right]. \quad (\text{B.3b})$$

After completing the square,

$$T = A_1 e^{\beta^2/\alpha} \int_{-(l/2)\sin\theta}^{(l/2)\sin\theta} \exp \left[-\alpha(\xi_1 - \beta/\alpha)^2 \right] d\xi_1, \quad (\text{B.4a})$$

where

$$\alpha = \frac{1}{4D_T t} + \frac{\cot^2 \theta}{4D_L t}, \quad \beta = \frac{\tilde{x}}{4D_T t} - \frac{(\tilde{z} - Vt) \cot \theta}{4D_L t}. \quad (\text{B.4b})$$

Change of the variable of integration, $\eta^2 = \alpha(\xi_1 - \beta/\alpha)^2$, yields

$$T = A_1 e^{\beta^2/\alpha} \frac{1}{\sqrt{\alpha}} \int_{\eta_-}^{\eta_+} e^{-\eta^2} d\eta = A_1 e^{\beta^2/\alpha} \frac{1}{\sqrt{\alpha}} \left[-\int_0^{\eta_-} e^{-\eta^2} d\eta + \int_0^{\eta_+} e^{-\eta^2} d\eta \right], \quad (\text{B.5})$$

where $\eta_{\pm} = -\beta/\sqrt{\alpha} \pm (\sqrt{\alpha}l/2)\sin\theta$. Rewriting this result in terms of the error function $\text{erf}(x) = (2/\sqrt{\pi}) \int_0^x \exp(-s^2) ds$ leads to (12).

B2. Periodic Point Source

Substituting this expression into (9) yields

$$T = \frac{E/(\rho c)}{8\pi^{3/2}\sqrt{D_L D_T}} \int_0^t \sin(\omega\tau) \frac{1}{(t-\tau)^{3/2}} \exp\left[-\frac{\tilde{x}^2 + \tilde{y}^2}{4D_T(t-\tau)} - \frac{(\tilde{z} - V(t-\tau))^2}{4D_L(t-\tau)}\right] d\tau. \quad (\text{B.6})$$

A change of the variable of integration, $\tau' = t - \tau$, gives (after relabeling $\tau' \mapsto \tau$)

$$T = \frac{E/(\rho c)}{8\pi^{3/2}\sqrt{D_L D_T}} \int_0^t \sin[\omega(t-\tau)] \frac{1}{\tau^{3/2}} \exp\left[-\frac{\tilde{x}^2 + \tilde{y}^2}{4D_T\tau} - \frac{(\tilde{z} - V\tau)^2}{4D_L\tau}\right] d\tau. \quad (\text{B.7})$$

Recalling that $\sin(a-b) = \sin a \cos b - \sin b \cos a$ leads to (13).

Acknowledgments

We thank M. Cardiff and the other two anonymous reviewers for their comments and suggestions. This work was supported in part by the National Science Foundation under grant CBET-1606192. There are no data sharing issues since all of the numerical information is provided in the figures produced by solving the equations in the paper.

References

- Anderson, M. P. (2005). Heat as a ground water tracer. *Ground Water*, 43, 951–968.
- Angermann, A. J., Lewandowski, J., Fleckenstein, H., & Nützmann, G. (2013). A 3D analysis algorithm to improve interpretation of heat pulse sensor results for the determination of small-scale flow directions and velocities in the hyporheic zone. *Journal of Hydrology*, 475, 1–11.
- Ballard, S., Barker, G. T., & Nichols, R. L. (1996). A test of the in situ permeable flow sensor at Savannah River, SC. *Ground Water*, 34, 389–396.
- Bear, J. (1972). *Dynamics of fluids in porous media*. New York: Elsevier.
- Boano, F., Harvey, J. W., Marion, A., Packman, A. I., Revelli, R., Ridolfi, L., et al. (2014). Hyporheic flow and transport processes: Mechanisms, models, and biogeochemical implications. *Reviews of Geophysics*, 52, 603–679. <https://doi.org/10.1002/2012RG000417>
- Boas, M. L. (2006). *Mathematical methods in the physical sciences* (3rd ed.). New York: Wiley.
- Bons, P. D., van Milligen, B. P., & Blum, P. (2013). A general unified expression for solute and heat dispersion in homogeneous porous media. *Water Resources Research*, 49, 6166–6178. <https://doi.org/10.1002/wrcr.20488>
- Burnett, R. D., & Frind, E. O. (1987). Simulation of contaminant transport in three dimensions: 2. Dimensionality effects. *Water Resources Research*, 23(4), 695–705.
- Cardiff, M., Bakhos, T., Kitanidis, P. K., & Barrash, W. (2013). Aquifer heterogeneity characterization with oscillatory pumping: Sensitivity analysis and imaging potential. *Water Resources Research*, 49, 5395–5410. <https://doi.org/10.1002/wrcr.20356>
- Cardiff, M., Liu, X., Kitanidis, P. K., Parker, J. C., & Kim, U. (2010). Cost optimization of DNAPL source and plume remediation under uncertainty using a semi-analytic model. *Journal of Contaminant Hydrology*, 113(1–4), 25–43.
- Ciriello, V., Bottarelli, M., Federico, V. D., & Tartakovsky, D. M. (2015). Temperature fields induced by geothermal devices. *Energy*, 93(2), 1896–1903. <https://doi.org/10.1016/j.energy.2015.10.052>
- Constantz, J., & Stonestrom, D. A. (2003). Heat as a tracer of water movement near streams. In D. A. Stonestrom & J. Constantz (Eds.), *Heat as a tool for studying the movement of ground water near streams U.S. Geological Survey Circular* (1260, pp. 1–7). Reston, VA: U.S. Geological Survey.
- Coutelieres, F. A., & Delgado, J. M. P. Q. (2012). *Transport processes in porous media*. New York: Springer.
- de Marsily, G. (1986). *Quantitative hydrology*. San Diego, CA: Academic Press.
- Farouki, O. T. (1986). *Thermal properties of soils, series on rock and soil mechanics* (Trans. Tech. Pub., Vol. 11). Rockport, MA.
- Gelhar, L. W., Welty, C., & Rehfeldt, K. R. (1992). A critical review of data on field-scale dispersion in aquifers. *Water Resources Research*, 28(7), 1955–1974.
- Hatch, C. E., Fisher, A. T., Revenaugh, J. S., Constantz, J., & Ruehl, C. (2006). Quantifying surface water? Groundwater interactions using time series analysis of streambed thermal records: Method development. *Water Resources Research*, 42, W10410. <https://doi.org/10.1029/2005WR004787>
- Hunt, B. (1978). Dispersive sources in uniform ground-water flow. *ASCE Journal of Hydraulic Division*, 104(HY1), 75–85.
- Ingebritsen, S. E., Sanford, W. E., & Neuzil, C. E. (2006). *Groundwater in geologic processes*. New York: Cambridge University Press.
- Irvine, D. J., Simmons, C. T., Werner, A. D., & Graf, T. (2015). Heat and solute tracers: How do they compare in heterogeneous aquifers? *Groundwater*, 53, 10–20.
- Labaky, W., Devlin, J. F., & Gillham, R. W. (2007). Probe for measuring groundwater velocity at the centimeter scale. *Environmental Science & Technology*, 41, 8453–8458.
- Lautz, L. K. (2010). Impacts of nonideal field conditions on vertical water velocity estimates from streambed temperature time series. *Water Resources Research*, 46, W01509. <https://doi.org/10.1029/2009WR007917>
- Lewandowski, J., Angermann, L., Nützmann, G., & Fleckenstein, J. H. (2011). A heat pulse technique for the determination of small-scale flow directions and flow velocities in the streambed of sand-bed streams. *Hydrological Processes*, 25, 3244–3255.
- Lichtner, P. C., Kelkar, S., & Robinson, B. (2002). New form of dispersion tensor for axisymmetric porous media with implementation in particle tracking. *Water Resources Research*, 38(8), 1146. <https://doi.org/10.1029/2000WR000100>
- Ong, J. B., & Zlotnik, V. A. (2011). Assessing lakebed hydraulic conductivity and seepage flux by potentiometer. *Groundwater*, 49(2), 270–274.
- Park, E., & Zhan, H. (2001). Analytical solutions of contaminant transport from finite one-, two-, and three-dimensional sources in a finite-thickness aquifer. *Journal of Contaminant Hydrology*, 53, 41–61.
- Rau, G. C., Andersen, M. S., & Acworth, R. I. (2012). Experimental investigation of the thermal dispersivity term and its significance in the heat transport equation for flow in sediments. *Water Resources Research*, 48, W03511. <https://doi.org/10.1029/2011WR011038>
- Rau, G. C., Andersen, M. S., McCallum, A. M., Roshan, H., & Acworth, R. I. (2014). Heat as a tracer to quantify water flow in near-surface sediments. *Earth Science Reviews*, 129, 40–58.
- Reeves, J., & Hatch, C. E. (2016). Impacts of three-dimensional nonuniform flow on quantification of groundwater-surface water interactions using heat as a tracer. *Water Resources Research*, 52, 6851–6866. <https://doi.org/10.1002/2016WR018841>
- Roshan, H., Rau, G. C., Andersen, M. S., & Acworth, R. I. (2012). Use of heat as tracer to quantify vertical streambed flow in a 2-D flow field. *Water Resources Research*, 48, W10508. <https://doi.org/10.1029/2012WR011918>

- Schneidewind, U., van Berkel, M., Anibas, C., Vandersteen, G., Schmidt, C., Joris, I., et al. (2016). LPMLE3: A novel 1-D approach to study water flow in streambeds using heat as a tracer. *Water Resources Research*, *52*, 6596–6610. <https://doi.org/10.1002/2015WR017453>
- Stallman, R. W. (1965). Steady one-dimensional fluid flow in a semi-infinite porous medium with sinusoidal surface temperature. *Journal of Geophysical Research*, *70*(12), 2821–2827.
- Suzuki, S. (1960). Percolation measurements based on heat flow through soil with special reference to paddy fields. *Journal of Geophysical Research*, *65*(9), 2883–2885.
- Yang, C., Sakai, M., & Jones, S. B. (2013). Inverse method for simultaneous determination of soil water flux density and thermal properties with a penta-needle heat pulse probe. *Water Resources Research*, *49*, 5851–5864. <https://doi.org/10.1002/wrcr.20459>
- Zech, A., Attinger, S., Cvetkovic, V., Dagan, G., Dietrich, P., Fiori, A., et al. (2015). Is unique scaling of aquifer macrodispersivity supported by field data? *Water Resources Research*, *51*, 7662–7679. <https://doi.org/10.1002/2015WR017220>
- Zhan, H., & Zlotnik, V. A. (2002). Groundwater flow to a horizontal or slanted well in an unconfined aquifer. *Water Resources Research*, *38*(7), 13.1–13.13. <https://doi.org/10.1029/2001WR000401>
- Zheng, C., & Bennett, G. (2002). *Applied contaminant transport modeling (2nd ed.)*. New York: John Wiley.
- Zlotnik, V. A., Kacimov, A. R., & Al-Maktoumi, A. (2017). Estimating groundwater mounding in sloping aquifers for managed aquifer recharge. *Groundwater*, *55*(6), 797–810.